JOURNAL OF CATALYSIS 137, 158–178 (1992)

Modeling Dynamic CO Oxidation over Pt/Al_2O_3: Effects of Intrapellet Diffusion and Site Heterogeneity

BERNARD N. RACINE AND RICHARD K. HERZ[1]

Chemical Engineering Group, Mail Code 0310, Department of Applied Mechanics and Engineering Sciences, University of California at San Diego, La Jolla, California 92093-0310

Received November 5, 1991; revised February 24, 1992

In this paper we have simulated both steady-state and time-resolved dynamic reaction measurements and directly compared them to experimental results. Effects such as internal diffusion resistance and site heterogeneity, which are commonly observed in supported metal catalysts, are included in the simulations presented here. Single-site Langmuir–Hinshelwood models fail to predict the rates of reaction measured during steady-state and dynamic operation. Both steady-state and time-resolved dynamic reaction measurements for two types of Pt/Al_2O_3 catalysts can be predicted by an elementary step model with a bimodal distribution of active sites. Diffusion resistance produced significant gas and surface concentration gradients inside the porous catalyst and suppressed the rate of CO_2 production during the initial period of CO-on half-cycles. To our knowledge, this is the first work comparing steady-state and time-resolved dynamic CO oxidation measurements to an elementary step model incorporating internal diffusion resistance.

INTRODUCTION

The CO oxidation reaction over supported noble metals often exhibits complex behavior: multiple steady states in reaction rate at intermediate CO pressures (*1–5*); self-sustained oscillations in reaction rate under constant feed conditions (*5–12*); and complex behavior during forced dynamic operation (*13–17*).

The general features of steady-state CO oxidation behavior over bulk, unsupported noble metals are understood reasonably well (*3, 18*). At fixed O_2 pressure and temperature and relatively low CO pressures, reaction rates are approximately first-order in CO pressure, O coverages are high, and CO coverages are low. At relatively high CO pressures, reaction rates become negative-order in CO pressure, O coverages are low, and CO coverages are high.

In contrast to the information available over bulk, unsupported noble metals, there are very few, if any, published experimental studies showing steady-state CO oxidation reaction rates over supported noble metals under (a) isothermal conditions, (b) in the absence of significant transport effects, and (c) covering both the positive-order-in-CO regime and the CO-inhibition regime. Most studies were performed either nonisothermally (*19–21*), near complete conversions when not in the CO-inhibition regime (*22, 23*), and/or with significant transport resistances (*2, 8*). Many infrared studies show only infrared absorbance plots, not steady-state reaction rates (*4, 24*). Cant *et al.* (*25*) and Oh *et al.* (*26*) studied isothermal kinetics over supported Pt-group metals in the CO-inhibition regime only. The papers that may come closest to presenting isothermal intrinsic kinetics that span both the positive-order and CO-inhibition regimes are those of Sarkany and Gonzalez (*27*), who measured rates over Pt/SiO_2 at 130°C and Akubuiro *et al.* (*28*), who measured rates over Pt on zeolite Y at 260°C.

Dynamic response experiments used in conjunction with steady-state reaction measurements provide stronger tests of kinetic models than steady-state measurements

[1] To whom correspondence should be addressed.

0021-9517/92 $5.00

alone. Dynamic operation also provides information concerning quantities of adsorbed intermediates and rates of forward and reverse steps in reaction mechanisms. The benefits of dynamic response methods were reviewed by Bennett (*29*) and Kobayashi and Kobayashi (*30*). Forced dynamic operation for CO oxidation over supported noble metal catalysts has been reviewed in detail in our previous work (*31*).

Conventional Langmuir–Hinshelwood kinetic models which assume random distribution of adsorbed species have been developed to simulate dynamic CO oxidation experiments over supported noble metals. Traditional textbook approaches often assume a single rate-limiting step in order to develop a simple algebraic rate expression. However, this assumption often breaks down during dynamic operation, where the rate-limiting step can change as concentrations change with time. A majority of the recent models of dynamic response experiments are elementary step models which do not assume a single rate-limiting step. Goodman *et al.* (*32*) used an elementary step random Langmuir–Hinshelwood model to describe CO oxidation transients over Pt/Al_2O_3. Kaul *et al.* (*19, 33*) used an elementary step model to describe the results of temperature and concentration-programming experiments over Pt/SiO_2. Lynch (*34*) also used an elementary step model to simulate rate enhancements for CO oxidation during periodic operation.

Spectroscopic evidence for segregation of adsorbed CO and O into surface patches and islands of adsorbed CO and O has been observed for CO oxidation under both steady-state and dynamic reaction conditions. The invariance of the linearly bonded CO infrared adsorption peak during steady-state reaction has been observed over both supported (*4, 35*) and nonsupported Pt catalysts (*36*). This frequency invariance has also been observed under dynamic reaction conditions over supported Pt catalysts (*15, 37*). This spectroscopic evidence has led various investigators to develop mathematical models of CO oxidation that specify the presence of adsorbate islands. A variety of adsorbate island models were used by Mukesh *et al.* (*38*) to model the transient data of Goodman *et al.* (*32*), with the model simulations being most sensitive to the presence of CO islands. Oscillatory behavior was also simulated with the same adsorbate island models, however, the types of oscillations were acknowledged to be different from those observed for CO oxidation over supported noble metal catalysts. Graham and Lynch (*39*) proposed a CO island model to predict steady-state rate multiplicity data. Monte Carlo simulations for CO oxidation have also predicted the formation of adsorbate islands under both steady-state (*40–42*) and transient conditions (*43–45*).

Schwartz and Schmidt (*46*) suggested that the Pt(100) hex-(1 × 1) surface phase transition observed by Ertl and co-workers (*11, 12, 47–49*) may be operative on polycrystalline wires and foils and on supported Pt particles. Schüth and Wicke (*50*) inferred from infrared measurements of the linear CO band the presence of the Pt(100) hex-(1 × 1) reconstruction during self-sustained oscillations of the CO–NO reaction over supported Pt. These observations have led researchers to adapt the reconstruction model of Ertl and co-workers (*11*) to explain oscillatory behavior observed for CO oxidation over supported metal catalysts. Lynch *et al.* (*51*) proposed sharp transitions in oxygen sticking coefficient for the hex-(1 × 1) transformation and (1 × 1)-hex transformation at high (θ = 0.95) and low (θ = 0.1) surface coverage values, respectively. These critical values of surface coverages are different from those determined by Ertl and co-workers for the Pt(100) phase transition (*48, 49*). A similar model was also used by Graham and Lynch (*23*) to explain both steady-state and forced composition cycling results for CO oxidation over Pt/Al_2O_3, except both the reaction rate constant and the oxygen sticking coefficient for the (1 × 1) phase were increased 250-fold to fit the experimental data.

The inclusion of intrapellet diffusion for dynamic response modeling of CO oxidation over supported metal catalysts is limited. Oh and Hegedus (*52*) studied the effects of both internal and external diffusion resistance on transient CO adsorption and desorption in the absence of reaction. Intrapellet concentration profiles suggest that steep profiles exist inside the catalysts during CO adsorption while relatively mild gradients are present during CO desorption. Oh, Hegedus, and Baron (*53*) directly compared dynamic CO oxidation experiments with theoretical predictions of a diffusion-limited reaction model, using an overall algebraic rate expression which assumes a single rate-determining step. Cho (*54*) developed an elementary step model of CO oxidation including intrapellet diffusion using Langmuir–Hinshelwood kinetics. The evolution of CO and oxygen surface coverage profiles in a porous catalyst during both steady-feed operation and forced concentration cycling were simulated, however, simulated CO_2 production rates were not directly compared to experimental time-resolved cycling measurements.

Mathematical models developed for CO oxidation have been used to fit both steady-state and dynamic behavior in only a few cases (*23, 32*). It is safe to say that a single comprehensive model of CO oxidation that describes all of the observed complex behavior has not yet been developed. Although previous forced-dynamic studies have demonstrated the complexity of CO oxidation over supported noble metals, the causes of the observed behavior are still unknown. Conclusive evidence to support the existence of patches or islands of adsorbed CO and O or metal crystallite surface reconstruction on supported metal catalysts is not available.

In previous work (*31*), we studied two Pt/Al_2O_3 samples prepared from chloride-containing and chloride-free Pt precursors and compared the behavior of the two catalysts in terms of their steady-state reaction behavior and dynamic responses to periodic changes of CO pressure in O_2. During dynamic reaction experiments at 145°C in the well-mixed reactor, CO pressures varied from 0 to 0.125 Torr at a constant O_2 pressure of 0.33 Torr over cycling periods of 24 s. The results of the steady-state and dynamic reaction experiments correlated with each other, indicating that the sample prepared from the chloride-free Pt precursor (tetraamineplatinum nitrate) had stronger CO–Pt interactions than the sample prepared from the chloride-containing Pt precursor (chloroplatinic acid). In this work, we compare directly the results of those steady-state and forced-dynamic CO oxidation experiments over Pt/Al_2O_3 to simulations accounting for internal diffusion using traditional single-site Langmuir–Hinshelwood kinetics for CO oxidation and a two-site model which explores the effects of site heterogeneity.

Our goals for this work were (1) to determine the effects of internal diffusion resistance on rapid dynamic rate measurements for CO oxidation, (2) to determine the suitability of a classic Langmuir–Hinshelwood mechanism to describe time-resolved measurements, and (3) to examine the possible effects of site heterogeneity on time-resolved reaction measurements. Our main conclusion is that a single mathematical model incorporating two types of active sites can explain the differences observed in both steady-state and dynamic behavior over the two catalysts studied.

To our knowledge, this is the first work comparing steady-state and time-resolved dynamic CO oxidation measurements to an elementary step model incorporating internal diffusion resistance.

MODEL EQUATIONS

The porous catalyst pellets represented in the simulations had slab geometry and were located in a well-mixed differential reactor (*31*). External mass transfer resistance was negligible at the low gas pressures and high reactant diffusivities present in the reactor. Because the CO pressure and conversion were very low (0.125 Torr and <3%, respec-

tively), temporal and spatial temperature variations in the catalyst pellets caused by the exothermic heat of reaction were negligible. In particular, CO pressures in the reactor were over 400 times lower than in studies of CO oxidation where large temporal and spatial temperature variations caused by the heat of reaction have been observed (*10, 55, 56*). The maximum amplitude of temperature variations measured by the thermocouples imbedded in the centers of our 5-mm diameter pellets during dynamic experiments was 1.0°C. Temperature gradients across the 0.38-mm thickness of the pellets were estimated to be ≤0.6°C.

The dimensionless mass balance equation for intrapellet fluid-phase CO is given by the expression

$$\alpha \frac{\partial c_{CO}}{\partial \tau} = \beta \frac{\partial^2 c_{CO}}{\partial x^2} - r_{aCO} + r_{dCO}. \quad (1)$$

Similarly, the dimensionless mass balance for intrapellet fluid-phase O_2 is given by the expression

$$\alpha \frac{\partial c_{O_2}}{\partial \tau} = \beta \frac{\partial^2 c_{O_2}}{\partial x^2} - r_{aO_2}. \quad (2)$$

Variables and parameters contained in the equations are defined in the Appendix. The desorption rate for oxygen is assumed to be negligible at the reaction temperature (145°C) for the dynamic experiments (*57*). The dimensionless mass balance for intrapellet fluid-phase CO_2 is given by the expression

$$\alpha \frac{\partial c_{CO_2}}{\partial \tau} = \beta \frac{\partial^2 c_{CO_2}}{\partial x^2} + r_{sr}, \quad (3)$$

where r_{sr} is the rate of the surface reaction between adsorbed CO and O. Figures 4 and 6a of our previous work (*31*) demonstrate that reversible adsorption of CO_2 onto the support is negligible, since the CO_2 concentration drops essentially as fast as the CO concentration when CO is switched off at 12 s into a cycle. In addition, we have performed experiments in which a mixture of CO_2 and Ar was switched on and off under conditions similar to those in (*31*). There was no apparent difference between the dynamic responses of CO_2 and Ar, confirming that CO_2 adsorption did not have a significant effect in our experiments.

The dimensionless mass balances for the surface species CO (θ_{CO}) and O (θ_O) are, respectively,

$$\frac{\partial \theta_{CO}}{\partial \tau} = r_{aCO} - r_{dCO} - r_{sr} \quad (4)$$

$$\frac{\partial \theta_O}{\partial \tau} = 2r_{aO_2} - r_{sr}. \quad (5)$$

Since the pellet is symmetrical about its centerplane, the dimensionless boundary conditions at centerplane of the pellet for each species i are

$$\frac{\partial c_i}{\partial x}(0, \tau) = 0. \quad (6)$$

The dimensionless boundary conditions at the external surface for this case are

$$c_{CO}(1, \tau) = f(\tau), \quad (7)$$

where $f(\tau)$ is defined by the CO vs time curve shown in Fig. 4 in (*31*), and

$$c_i(1, \tau) = c_i^O \quad (8)$$

for O_2 and CO_2. The reactor is a differential reactor (conversion <3%), so $c_{CO_2}^O$ was set equal to zero.

Since the time-resolved measurements shown in this paper are average cycles, the profiles at $t = 0$ s and $t = 24$ s must match. Therefore, the dimensionless initial conditions are defined as the conditions which exist inside the pellet at $t = 24$ s which match the initial conditions at $t = 0$ s from the same cycle.

The system of partial differential equations in Eqs. (1)–(5) was solved using the method of lines with cubic Hermite polynomials. Time is made dimensionless using the reaction rate constant. The values of gas concentrations, pellet half-thickness, void fraction, diffusivity, and "gas-to-surface capacity ratio" were either measured directly

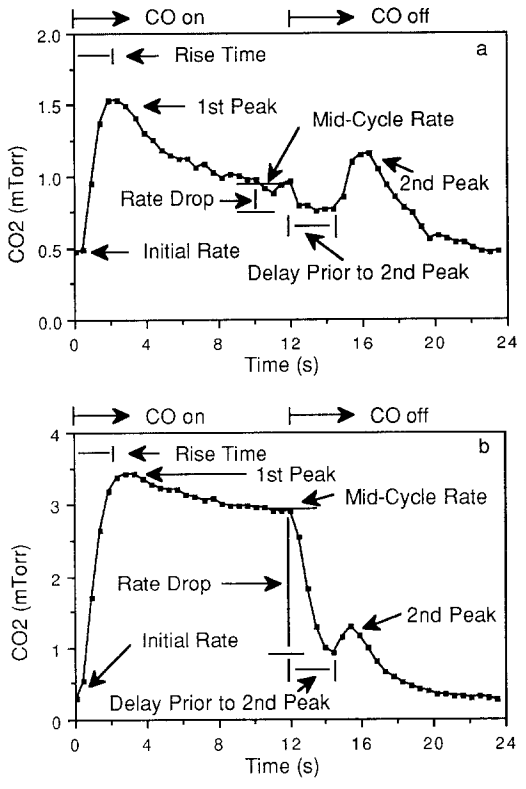

FIG. 1. Key features of the dynamic CO_2 responses of Pt/Al_2O_3 catalysts prepared from (a) tetraamineplatinum nitrate ("nitrate sample") and (b) chloroplatinic acid ("chloride sample") over a 24-s cycle. The CO pressure was periodically cycled between 2 and 120 mTorr with a 50% duty fraction, while the O_2 pressure was held constant at 330 mTorr. A single cycle is shown for each catalyst which is the average of 20 successive cycles. The vertical scales show the CO_2 concentration in the well-mixed reactor which is proportional to the overall rate of CO_2 production. The catalyst temperature was 145°C.

or estimated from mercury porosimetry and chemisorption uptake measurements. The rate parameter values used in the simulations were chosen based on appropriate fits of the dynamic responses shown in Fig. 1.

The instantaneous dimensionless rate of diffusion of CO_2 out of the pellet is

$$r_{CO_2} = -\beta \left[\frac{\partial c_{CO_2}}{\partial x} \right]_{x=1}. \qquad (9)$$

Since CO_2 is a nonadsorbing species in the model, its diffusion time constant is on the order of milliseconds. Therefore the CO_2 intrapellet profile is in quasi-steady state at all times such that Eq. (9) simply integrates the local surface reaction rate r_{sr} over the pellet. Use of a different diffusivity for CO_2 will not affect the results since the concentration gradient will compensate and result in no change in the rate of diffusion of CO_2 out of the pellet.

For comparison to experimental measurements, the concentration of CO_2 at the outlet of the differential reactor is calculated from the instantaneous rate of diffusion of CO_2 out of the pellet through application of an exponential lag due to bulk gas mixing in the reactor. In (*31*) the mean gas residence time in the reactor system was specified as 1.0 s. This is the mean residence time for gas molecules diffusing from the piezoelectric valves through a six-way cross into the reactor chamber, where gas concentrations are measured by the mass spectrometer. The volume of the six-way cross and adjoining connections was approximately one-fourth of the total volume of the six-way cross and reactor chamber. Simulations indicated that molecules diffusing out of the pellet and flowing out of the reactor chamber were lagged with an exponential time constant of only 0.7 s, the time constant used for the results presented here. The calculation of a finite outlet concentration does not conflict with the boundary condition at the external surface for gas phase CO_2 set above, since CO_2 is a nonadsorbing species which does not participate in any reactions and diffuses rapidly such that its intrapellet profile is in quasi-steady state at all times.

RESULTS AND DISCUSSION

Key Features of Dynamic Experiments

Figure 1 shows the key qualitative features of the dynamic experiments which we took as the criteria for modeling. The dynamic experiments performed previously (*31*) consist of a 24-s cycle with a 50% duty fraction of CO in constant oxygen at constant temperature. Data was acquired and

averaged over 20 cycles, with 5 cycles elapsed prior to data acquisition. The vertical scales show the CO_2 concentration in the well-mixed reactor which is proportional to the overall rate of CO_2 production.

Two types of Pt/Al_2O_3 catalysts from different platinum precursors were studied, one prepared from chloroplatinic acid (chloride sample) and one prepared from tetraamineplatinum nitrate (nitrate sample). Comparison of Figs. 1a and 1b reveals that the nitrate and chloride sample dynamic responses have the same seven key features which need to be modeled. First is the initial rate of CO_2 production, which is equivalent to the final rate at 24 s since average cycles are shown. The initial rate for both the chloride and nitrate samples is nonzero due to nonzero background CO levels in the reactor during the CO-off half-periods. The second key feature is the rate of increase in CO_2 pressure ("rise time" in Figs. 1a and 1b) when CO is switched on. Next is the peak height for the first peak. The mid-cycle rates at 12 s, where both CO and oxygen are present in full concentrations, are nonzero for both catalysts and must be accurately predicted. The nonzero mid-cycle rates for both catalysts indicate that CO and oxygen coexist on the surface at 12 s.

The most difficult features to model are the decline in CO_2 production and the time delay prior to formation of the CO_2 peak in the CO-off half-period of the cycle. The decline in CO_2 production when CO is switched off at 12 s is the most important feature in both dynamic responses shown in Fig. 1. The discussion to follow will demonstrate that traditional models of CO oxidation cannot predict the decline in CO_2 production preceding the second CO_2 peak.

The final key feature to model is the second CO_2 peak height and shape in the CO-off half-period of the cycle. In addition to fitting the various features of the dynamic response data, each kinetic model should predict observed steady-state rate data for both samples in order to provide a more complete test of the model.

Classic Langmuir–Hinshelwood (L–H) Model

The assumptions implicit in this model are as follows:

1. All surface sites are identical.
2. There is no interaction between adsorbed species other than reaction.
3. Adsorbed species are randomly distributed over the array of sites.
4. CO and O_2 compete for the same adsorption sites.
5. CO adsorbs molecularly and O_2 adsorbs dissociatively as O.
6. Adsorbed CO and adsorbed O each take up one site.
7. CO_2 is weakly adsorbed and surface coverages of CO_2 are negligible.

The kinetic equations resulting from assumptions 1 through 7 are often used to model steady-state CO oxidation behavior (*58*).

For the classic Langmuir–Hinshelwood mechanism, the elementary reaction steps for CO adsorption, O_2 adsorption, CO desorption, and surface reaction, respectively, are defined by the expressions

$$r_{aCO} = \gamma_{aCO} c_{CO}(1 - \theta_{CO} - \theta_O) \quad (10)$$

$$r_{aO_2} = \gamma_{aO_2} c_{O_2}(1 - \theta_{CO} - \theta_O)^2 \quad (11)$$

$$r_{dCO} = \gamma_{dCO} \theta_{CO} \quad (12)$$

$$r_{sr} = \theta_{CO} \theta_O . \quad (13)$$

The fractional surface coverages θ_i shown in Eqs. (10)–(13) above are defined in the Appendix as the number of surface sites occupied by species i divided by the number of surface sites of species i at saturation. Since time was made dimensionless using the surface reaction rate constant, a dimensionless rate constant does not appear in the surface reaction rate expression.

The classic model only allows one to match only two out of seven features of the dynamic data. Figure 2 shows a fit of the classic L–H model to the nitrate sample data shown in Fig. 1a. The criteria for fitting the

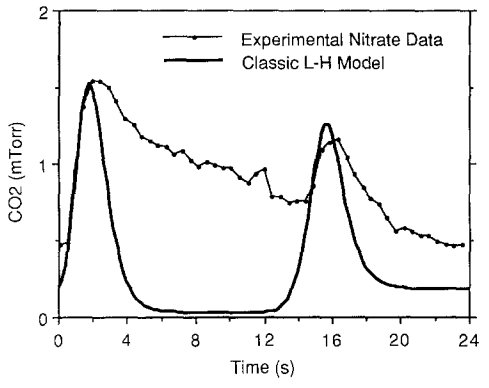

FIG. 2. Comparison of the simulated dynamic response of the classic Langmuir–Hinshelwood model to the experimental CO_2 response shown in Fig. 1 for the nitrate sample. Dimensionless rate constants used are $\gamma_{aCO} = 9.738 \times 10^3$, $\gamma_{aO_2} = 3.25$, and $\gamma_{dCO} = 57.7$.

data was based on the following characteristics shown in Fig. 1: the initial rise time and the height of the first CO_2 peak. The best fit response in Fig. 2 is obviously inadequate, since the model fails completely to predict the CO_2 level at 12 s. In order to match the initial rise time, the classic model requires a large ratio of CO sticking coefficient to oxygen sticking coefficient, which results in adsorbed CO saturating the surface of the catalyst. Under steady-state conditions, this drives the reaction into severe inhibition at relatively low CO pressures (>0.03 mTorr). The model can predict a nonzero initial rate equal to that observed experimentally, however, this requires use of an even larger ratio of CO to oxygen sticking coefficient. For these parameters, however, the resulting increase in CO_2 pressure when CO is switched on is greater than that obtained experimentally. Decreasing the rise time can be achieved by increasing the rate of CO desorption, however, this results in a reduced initial rate (the same effect as lowering the ratio of sticking coefficients).

One could match the steady-state CO_2 level at 12 s using parameters which yield less negative-order intrinsic steady-state kinetics, however the resulting dynamic response would not yield any peaks, only a gradual increase in rate to the experimental CO_2 level at 12 s, followed by a gradual decline in rate after CO is switched off. Similar arguments can be used to describe the failure of the classic L–H model in describing the chloride sample's dynamic response behavior, with marked failures in modeling the rise time, the decline in rate following flushing of CO from the reactor, and the second CO_2 peak.

Modified Single-Site L–H Model

The classic Langmuir–Hinshelwood model assumes that adsorbed O inhibits CO adsorption, but previous studies (*16, 37, 59, 60*) of induction times for CO exposed to supported noble metals covered with preadsorbed oxygen have shown that adsorbed oxygen does not significantly inhibit CO adsorption. Modification of the classic model to account for these experimental observations can be done in several ways, for example, by specifying that saturation coverage of oxygen does not cover all CO adsorption sites (*58*) or by adding an Eley–Rideal step (*61*). Such a modification can provide an improvement over the response of the classic model by allowing rapid production of CO_2 at the start of a cycle without driving the system far into the CO-inhibition regime after the first CO_2 peak.

Uncertainties also exist concerning the details of O_2 adsorption kinetics during CO oxidation. Tsai *et al.* (*62*) have shown that it is difficult to reconcile observations that CO oxidation rates in the inhibition regime depend only on CO/O_2 ratio and not on total pressure, suggesting a first-order dependence of O_2 adsorption on vacant sites, with the presence of intrinsic rate multiplicities and oscillations, which seem to require the nonlinearity provided by a second-order dependence of O_2 adsorption on vacant sites. Harold and Garske (*61*) have shown that a second-order dependence of O_2 adsorption on vacant sites leads to a negative second-order dependence on CO partial pressure when O_2 adsorption is assumed to be the

rate-limiting step, whereas the experimentally observed dependence is negative first-order or less. Changing the classic L–H model so the rate of O_2 adsorption is first-order in vacant sites might provide a better fit to our data since the rate would not be suppressed as much after the first CO_2 peak.

Here, we have chosen to modify the classic L–H model in order to account for the experimental observations that preadsorbed oxygen does not significantly inhibit CO adsorption by changing r_{a1} and r_{a2} to

$$r_{aCO} = \gamma_{aCO} c_{CO}(1 - \theta_{CO}) \quad (14)$$

$$r_{aO_2} = \gamma_{aO_2} c_{O_2}(1 - (1 - \theta_O)\theta_{CO} - \theta_O)^2. \quad (15)$$

Now, only adsorbed CO inhibits CO adsorption. The rate of oxygen adsorption is still proportional to the square of the number of free sites available, however, the formulation for this becomes $(1 - (1 - \theta_O)\theta_{CO} - \theta_O)^2$. The term $(1 - \theta_O)\theta_{CO}$ represents the fraction of sites not covered by oxygen which are covered by CO. Sites are available for O_2 adsorption until either θ_{CO} or θ_O reaches saturation coverage. An experimental study providing additional support for the use of such rate expressions was provided by Conrad *et al.* (*63*), who observed mixed phases of adsorbed CO and O on single-crystal Pd under nonreaction conditions with greater surface densities than single component layers of either CO or O.

This modified L–H model is a small improvement over the classic L–H model, since it can fit four out of the seven features of the dynamic data. Figure 3 shows a fit of the nitrate data with the modified L–H model. The modified L–H model can fit all four of the features of the initial peak, the initial rate, the rise time, the first peak height, and the mid-cycle rate, as demonstrated in Fig. 3. The modified L–H model predicts a nonzero surface coverage of CO near the external surface of the pellet at the background CO pressure (approx. 2 mTorr) in the reactor at 24 s during each cycle (*31*).

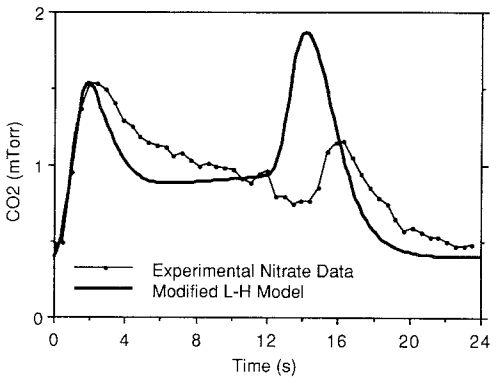

FIG. 3. Comparison of the simulated dynamic response of the modified Langmuir–Hinshelwood model to the experimental CO_2 response shown in Fig. 1 for the nitrate sample. Dimensionless rate constants used are $\gamma_{aCO} = 1.055 \times 10^4$, $\gamma_{aO_2} = 2.109 \times 10^3$, and $\gamma_{dCO} = 31.25$.

The nonzero coverage of CO results from the lack of inhibition of CO adsorption by oxygen, despite the relatively low CO to oxygen adsorption rate constant ratio used for the simulation. This low ratio still allows a rapid rise in rate since CO adsorption is not inhibited by adsorbed O, and also results in a nonzero rate at high CO pressures (unlike the classic L–H model which shows almost complete inhibition from 6–12 s during the cycle).

However, even the modified L–H model was unable to predict the dynamic behavior of the catalyst after CO was switched off. The model predicts neither the decrease in CO_2 pressure after CO is switched off, nor predicts the peak height nor location of the second peak. In addition, the model fails to predict the zero-order steady-state behavior for the nitrate sample, as shown in Fig. 4.

The failure of both of the classic and modified L–H models is inherent due to the fact that CO_2 peaks can only result from maximums in the product of surface coverages, $\theta_{CO}\theta_O$. To predict the first peak, the model must pass through a maximum in $\theta_{CO}\theta_O$, resulting in a majority of the surface covered with CO. Both CO and oxygen coexist on the surface at 12 s for the modified L–H

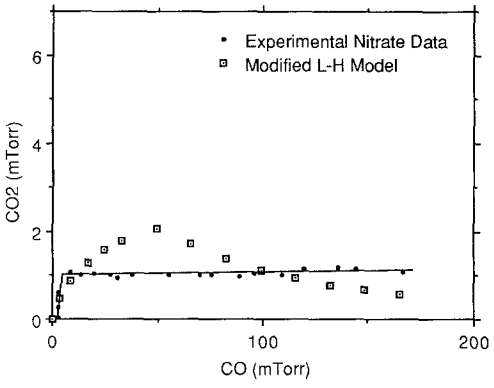

FIG. 4. Comparison of the modified L–H model predictions to the experimental steady-state data for the nitrate sample at 145°C and 330 mTorr O_2. Dimensionless rate constants used are $\gamma_{aCO} = 1.055 \times 10^4$, $\gamma_{aO_2} = 2.109 \times 10^3$, and $\gamma_{dCO} = 31.25$.

model, resulting in the predicted nonzero mid-cycle rate shown in Fig. 3. However, once CO is switched off, the surface coverage of oxygen starts increasing immediately, resulting in an immediate increase in CO_2 rate which continues until a second maximum in $\theta_{CO}\theta_O$ occurs.

Therefore, after CO is switched off, neither the classic L–H model nor the modified model can predict the key feature of the experimental data: the decrease in CO_2 rate preceding the formation of the second CO_2 peak. This would be the case even if additional modifications were made to make the oxygen adsorption rate first-order in vacant sites.

To demonstrate this failure of the modified L–H model, Fig. 5 shows the range of responses possible for the cycled-CO experiment. Figure 5 shows a series of dynamic response curves as a function of CO desorption rate. Identical CO adsorption, oxygen adsorption, and reaction rates are used for each curve. At low desorption rates (curve (d)), CO quickly dominates the surface of the catalyst, resulting in initial peaks in rate of CO_2 production; then, as CO pressures at the external surface increase during the cycle, the rate is driven into inhibition. Since the coverage of CO is high and oxygen coverage is very low at 12 s, when CO is switched off, the rate increases immediately as oxygen adsorbs on the surface and reacts away CO, forming a second peak. As the CO desorption rate increases, relative coverages of CO are lower, the initial peak shifts to later times, and the rate at 12 s is higher, due to increased surface coverage of oxygen. Since more oxygen is present on the surface at 12 s, the surface requires less time to reach a maximum in rate after CO is switched off. This results in the second peak shifting to earlier times during the cycle.

Because diffusion resistance slows the adsorption of CO when CO is switched on, the second peak maximum is higher in rate than the first peak for these modified L–H model simulations. This also results in the initial peak disappearing prior to the second peak (as shown by curve (b), $\gamma_{dCO} = 125$). When the desorption rate is sufficiently high (curve (a), $\gamma_{dCO} = 250$), the intrinsic kinetics are sufficiently positive order so as to remove both peaks altogether. Diffusion does not significantly affect the CO-off half-period of the cycle since both CO and oxygen are already present on the surface inside the catalyst when CO is switched off.

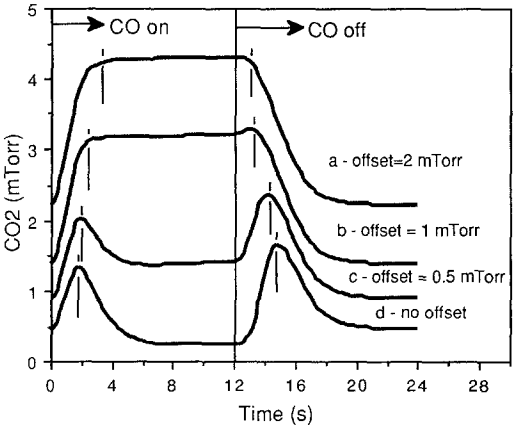

FIG. 5. Characteristic dynamic CO_2 responses of the modified L–H model (single-site model). All curves have the following parameter values: $\gamma_{aCO} = 1.055 \times 10^4$ and $\gamma_{aO_2} = 2.109 \times 10^3$. For curve (a) $\gamma_{dCO} = 250$; (b) $\gamma_{dCO} = 125$; (c) $\gamma_{dCO} = 31.25$; (d) $\gamma_{dCO} = 12.5$.

Bimodal Site Distribution Model—"Two-Site" Model

In (*31*) we proposed that simple L–H kinetics combined with a distribution of sites with different CO adsorption energies might explain the zero-order steady-state behavior observed over the nitrate sample. The range of behavior for dynamic responses shown in Fig. 5 for the modified L–H model using a single type of adsorption site supports the proposal that a distribution of surface sites might also predict the dynamic behavior shown in Fig. 1. The simulated dynamic response of a single-site model for a high rate of CO desorption (Fig. 5a) results in an increase in CO_2 production after CO is turned on without formation of the first CO_2 peak. Since the product $\theta_{CO}\theta_O$ does not go through a maximum, the second CO_2 peak is also not formed after CO is turned off. For a lower CO desorption rate (Fig. 5d), two CO_2 peaks are formed: the first caused by rapid CO adsorption and reaction followed by inhibition at high CO pressures, and the second by reaction of adsorbed CO after CO is switched off. Addition of the dynamic responses shown in Fig. 5a (which predicts a nonzero mid-cycle rate) and Fig. 5d (which predicts formation of two CO_2 peaks), in some relative ratio, would appear to provide a response containing the first CO_2 peak, a nonzero mid-cycle rate, and a drop in rate followed by the second CO_2 peak. This suggests that a model incorporating multiple adsorption sites with different activities might yield dynamic responses similar to those seen experimentally.

Supported metal particles have a variety of different crystal planes and metal surface structures exposed on their surfaces (*46, 64*). Crystallite size has been shown to affect crystallite shape and exposed crystal faces for noble metal catalysts (*65*). Particle size and particle size distribution affect crystal faces which are exposed for adsorption (*66*). TPD spectra have shown different crystal faces to have different CO adsorption characteristics (*67*). Particle size also affects CO bonding configurations for noble metal catalysts. Adsorption of CO in a bridge-bonded configuration is favored on large Pt particles and linearly bonded CO is favored on small Pt particles (*27*), with the bridge-bonded species having a lower binding energy (*68*) and greater reactivity (*27*). Bonding configurations have also shown coverage dependence on model Pd catalysts (*69*).

Our previous work demonstrated that CO adsorption strength can be directly correlated with both steady-state and dynamic reaction characteristics (*31*). Investigations of this nature support the assertion that supported noble metal catalysts used for CO oxidation have multiple types of adsorption sites with different reactivities. Yao *et al.* (*70*) found that Pt oxide deposited on Al_2O_3 was present in two phases: a particulate phase with little interaction with the support and a dispersed phase with larger support interactions. Oukaci *et al.* (*71*), through analysis of steady-state isotopic tracing experiments during CO oxidation, concluded that the distributions of active sites in their supported Rh, Pt and Rh/Pt catalysts were bimodal. Sant and Wolf (*10*) found that oscillations for CO oxidation over Pt/SiO_2 are a function of the size distribution and spacing of Pt crystallites. Oscillations for catalysts with bimodal particle size distributions were attributed to good communication between small crystallites closely spaced together. This communication, however, was hindered by heat conduction limitations in the catalyst.

The idea of multiple types of adsorption sites with different reactivities has not been invoked in previous mathematical models of CO oxidation. Below, we demonstrate that our observed dynamic and steady-state behavior for both supported Pt/Al_2O_3 catalysts can be explained with a single model which specifies two distinct types of adsorption sites with different adsorption characteristics and reactivities.

The bimodal site distribution model (two-site model) specifies that active sites are di-

vided into two types of sites which have different adsorption and reaction characteristics. The two types of sites are assumed to be independent of each other, that is, there is no interaction between adsorbed species on different types of sites.

Single-site models applied to supported metal catalysts often implicitly assume that rate constants represent average properties of a distribution of sites with different properties. This assumption works as long as the distribution of sites is unimodal and not too broad. In our two-site model, we expect that there are not necessarily two unique types of sites but rather a bimodal distribution of sites with average rate parameters corresponding to each peak in the distribution. A distribution of sites can result even when all particles are the same size since multiple facets may be exposed on each supported metal crystallite.

The dimensionless gas phase species equations retain the same form as those shown in Eqs. (1)–(3) except that the CO adsorption rate, CO desorption rate, O_2 adsorption rate, and reaction rate are now a summation of the product of the individual rates over N types of sites (where $N = 2$ here) multiplied by the fraction of each type of site. For example, the CO adsorption rate in Eqs. (1)–(3) becomes

$$r_{\mathrm{aCO}} = \sum_{j=1}^{N} f_j r_{\mathrm{aj CO}}, \tag{16}$$

where f_j represents the fraction of total sites which are type-j sites, and where the sum of all f_j equals 1. Similarly, all of the rates given in Eqs. (1)–(3) become sums of rates. The accumulation and diffusion terms for the gas-phase species remain the same as in Eqs. (1)–(3).

Mass balance equations are required each of the four surface species. The two surface CO equations each have the same functional form as Eq. (4) and the two surface oxygen each have the same functional form as Eq. (5). The surface CO balances for the two-site model are given by the expression

$$\frac{\partial \theta_{j\mathrm{CO}}}{\partial \tau} = r_{\mathrm{aj CO}} - r_{\mathrm{dj CO}} - r_{\mathrm{sr}j}, \tag{17}$$

and the surface oxygen balances for the two-site model are

$$\frac{\partial \theta_{j\mathrm{O}}}{\partial \tau} = 2r_{\mathrm{aj O_2}} - r_{\mathrm{sr}j} \tag{18}$$

where $j = 1$ for type-1 sites and $j = 2$ for type-2 sites. The rate expressions are

$$r_{\mathrm{aj CO}} = \gamma_{\mathrm{aj CO}} c_{\mathrm{CO}} (1 - \theta_{j\mathrm{CO}}) \tag{19}$$

$$r_{\mathrm{aj O_2}} = \gamma_{\mathrm{aj O_2}} f_j c_{\mathrm{O_2}} (1 - (1 - \theta_{j\mathrm{O}})\theta_{j\mathrm{CO}} - \theta_{j\mathrm{O}})^2 \tag{20}$$

$$r_{\mathrm{dj CO}} = \gamma_{\mathrm{dj CO}} \theta_{j\mathrm{CO}} \tag{21}$$

$$r_{\mathrm{sr}j} = \gamma_{\mathrm{sr}j} f_j \theta_{j\mathrm{CO}} \theta_{j\mathrm{O}}. \tag{22}$$

Oxygen does not inhibit CO adsorption, as was specified in the modified L–H model. The fractional surface coverages θ_{ij} are defined as the number of type-j sites occupied by species i divided by the number of type-j sites occupied by species i at saturation. Time is made dimensionless by the surface reaction rate constant for type-1 sites. The choice of this rate constant to make the equations dimensionless is arbitrary; other appropriate choices of scaling times can be made.

The equations for the two-site model were solved to obtain fits of the dynamic CO_2 responses for the nitrate and chloride samples based on the criteria in Fig. 1. Model predictions of steady-state data were obtained by specifying various constant pressures of CO at the external surface of the pellet and then integrating the equations to steady state at each pressure. No hysteresis in steady-state rate was observed in the experiments or simulations over the range of conditions studied. For a given sample, the same values of model parameters were used for both the dynamic and steady-state simulations. The values of the rate parameters used for the simulations are listed in Table 1.

TABLE 1

Parameters for Two-Site Model Used in Simulations

Parameter (description)	Nitrate sample (Figs. 6–7)	Chloride sample (Figs. 8–12)
γ_{a1CO} (CO ads, site 1)[a]	4.219×10^3	2.813×10^3
γ_{a2CO} (CO ads, site 2)[a]	4.219×10^3	2.813×10^3
γ_{a1O_2} (O_2 ads, site 1)[a]	8.437×10^2	5.625×10^2
γ_{a2O_2} (O_2 ads, site 2)[a]	8.437×10^2	5.625×10^2
γ_{d1CO} (CO des, site 1)	1.25	0.67
γ_{d2CO} (CO des, site 2)	150	500
γ_{sr1} (reaction, site 1)	1	1
γ_{sr2} (reaction, site 2)	1	2.16
f_1, f_2 (fraction of sites)	0.6, 0.4	0.5, 0.5

[a] k_{sr1} (chloride) = 1.5 k_{sr1} (nitrate), so k_{aji} (chloride) = k_{aji} (nitrate).

The two types of sites specified for the nitrate simulation differ only in their adsorption strengths for CO, with each type of site having the same reactivity. The two types of sites have equal sticking coefficients for CO, but differ in their desorption rates for CO (γ_{d1CO} = 1.25 and γ_{d2CO} = 150). The proportion of sites for the nitrate simulations is 60% type-1 sites (stronger CO adsorption) and 40% type-2 sites (weaker CO adsorption). The rate parameters α, β, γ_{a1CO}, γ_{a1O_2}, γ_{a2CO}, and γ_{a2O_2} were taken as adjustable parameters in this work. For the values of these parameters given in Table 1, the corresponding values of Pt loading, dispersion, effective diffusivity, and sticking coefficients for CO and oxygen are each within a factor of five of estimates obtained from CO TPD and mercury porosimetry measurements and published estimates of sticking coefficients.

Figure 6 shows the two-site model predicts the initial peak in the dynamic response and the features of the second peak as well. In contrast to Fig. 3 (single-site model simulation), the two-site model predicts a decrease in CO_2 rate after CO is switched off, reaching a minimum at t = 14.5 s before increasing to a peak maximum at t = 16 s. This is consistent with the data observed experimentally. The decline in rate results from the contribution of positive-order reaction over type-2 sites, whose CO coverage declines after CO is switched off. The magnitude of the second peak predicted by the two-site model is also more consistent with the data than the single-site model. Following the second CO_2 peak, the reaction rate decreases, leveling off at a nonzero value at 24 s. The nonzero rate is due to the residual CO pressure in the reactor at 24 s.

The comparison between the steady-state CO_2 rates predicted for the single-site and two-site models is interesting. In Fig. 4, the single-site model exhibits classic behavior for CO oxidation: positive-order in CO at low CO pressures and negative-order in CO at high CO pressures. The steady-state data for the two-site model, shown in Fig. 7, is remarkably consistent with the experimental data for the nitrate sample. The rate is positive-order in CO at low pressures (<10 mTorr), followed by a zero-order region at pressures greater than 25 mTorr CO. Type-1 sites are nearly saturated with CO at pressures greater than 25 mTorr, resulting in a declining rate of CO_2 production on type-1 sites as oxygen coverage decreases with increasing CO pressure. This decline in rate on type-1 sites is offset by positive-order behavior on type-2 sites at pressures greater

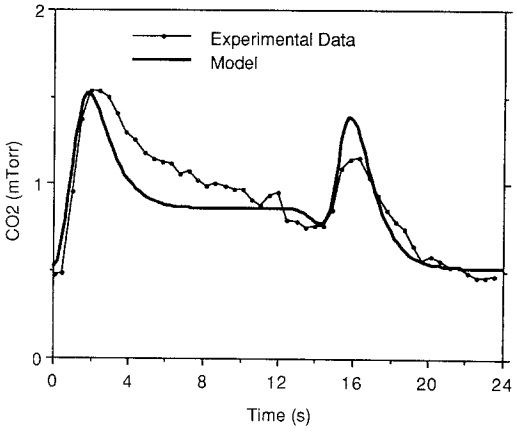

FIG. 6. Comparison of simulated dynamic response of the two-site model to the experimental CO_2 response shown in Fig. 1 for the nitrate sample. Dimensionless parameters for the simulation are listed in Table 1.

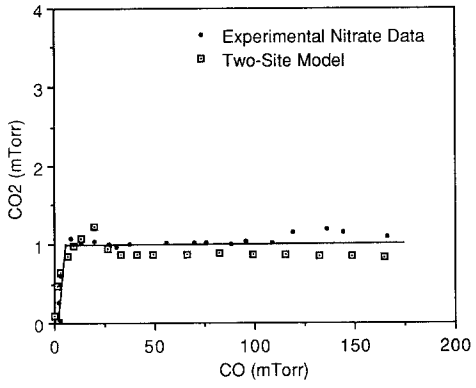

FIG. 7. Comparison of the two-site model predictions to the experimental steady-state data for the nitrate sample at 145°C and 330 mTorr O_2. Dimensionless parameters for the simulation are listed in Table 1.

than 25 mTorr. The result is an overall CO_2 production rate which appears zero-order over the range of CO pressures studied.

In Fig. 1, the dynamic response of the chloride sample is similar to the dynamic response of the nitrate sample, with some differences. The drop in CO_2 production rate from the first CO_2 peak to the rate at 12 s is not as large over the chloride sample. The decline in rate after CO was switched off is more pronounced for the chloride sample and the size of the second peak at 15.5 s is much smaller.

Despite these differences, the dynamic response of the chloride sample can also be modeled using the two-site model, as shown in Fig. 8. The simulation results closely match the initial rate, the peak size at 3.5 s, the rate of decline in CO_2 pressure after CO was switched off, and the peak at 15.5 s.

The largest discrepancy in the dynamic predictions of the model, for both the chloride and nitrate simulations, is the rate of decline following the first CO_2 peak at 3.5 s. Overall, however, there is excellent agreement between the experimental data and the model predictions of the dynamic responses. The two-site model predicts the observed dynamic behavior for both Pt/Al_2O_3 catalysts with the specification of only three additional parameters: the fraction of the second type of site, a new reaction rate constant for the second type of site, and a new CO desorption rate constant for the second type of site.

Previous TPD and adsorption calorimetry measurements suggested that the chloride sample adsorbs CO more weakly than the nitrate sample (*31*). The parameters used for the chloride simulation are consistent with this observation. Type-2 sites in the chloride simulation adsorb CO more weakly than type-2 sites in the nitrate simulation (γ_{d2CO}(chloride) > γ_{d2CO}(nitrate)). The larger reaction rate constant over type-2 sites in the chloride simulation accentuates the effects of the weaker CO adsorption over these sites.

Figure 9 shows the comparison of the simulation results to the steady-state data for the chloride sample. The two-site model predicts positive-order behavior in CO pressure over the range of CO pressures studied, although the agreement between model and experimental data is not as good as the agreement for the nitrate sample shown in Fig. 7. The less than first-order behavior of the simulated steady-state data in Fig. 9 is attributed mainly to the lack of inhibition of CO adsorption by adsorbed oxygen in the modified L–H models: the surface reaction

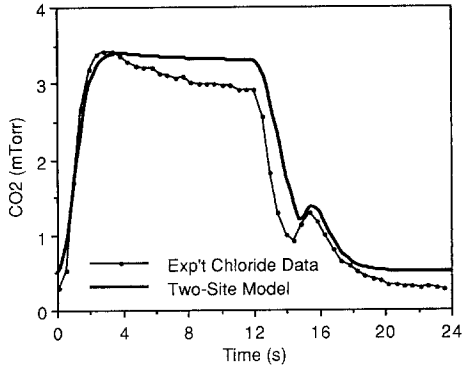

FIG. 8. Comparison of simulated dynamic response of the two-site model to the experimental CO_2 response shown in Fig. 1 for the chloride sample. Dimensionless parameters for the simulation are listed in Table 1.

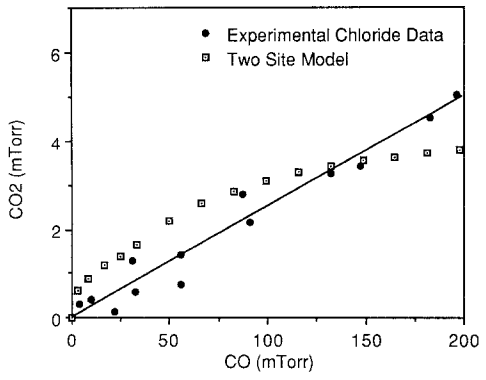

FIG. 9. Comparison of the two-site model predictions to the experimental steady-state data for the chloride sample at 145°C and 330 mTorr O_2. Dimensionless parameters for the simulation are listed in Table 1.

rate is proportional to the product of the oxygen and CO coverages and the CO coverage is roughly proportional to $KP_{CO}/(1 + KP_{CO})$. There are several ways in which the steady-state predictions of the model might be improved. For example, the classic L–H model, where each adsorbed oxygen atom excludes CO from adsorbing on that site, yields greater than first-order steady-state behavior in CO pressure in the positive-order regime (*62*). "Mixing" the two expressions for CO adsorption in the modified and classic L–H models by allowing some inhibition of CO adsorption by adsorbed oxygen would result in more linear steady-state behavior for the chloride simulation (*58*).

Some debate exists over whether CO oxidation over supported Pt is structure sensitive. Most studies have found some structure dependence for rates of CO oxidation. McCarthy *et al.* (*72*) observed CO oxidation to be demanding at low CO concentrations and facile at high CO concentrations over Pt/Al_2O_3. Akubuiro *et al.* (*28*) found that demanding behavior is observed at both high and low concentrations when Pt crystallites have average diameters less than 3 nm. Lower activities were noted at small crystallite sizes by Herskowitz *et al.* for supported Pt catalysts (*73*). In contrast, Cant (*74*) observed no clear dependence of turnover number on metal dispersion for CO oxidation over Pt/SiO_2. Sarkany and Gonzalez (*27*) also found CO oxidation rates over Pt/SiO_2 to be relatively insensitive to dispersion, but turnover numbers increased with decreasing dispersion over Pt/Al_2O_3. The degree of structure sensitivity appears to be a function of gas concentrations, as well as particle size and supports used.

In addition, the degree of structure sensitivity should be a function of temperature, given the differences in activation energy for desorption over different Pt crystal faces (*67*). In one sample with a bimodal site distribution, the relative activities of the two types of sites should change dramatically in the 50 to 200°C temperature range, with one type of site switching into a positive-order region and the other type of site remaining in the inhibition region. Similarly, the relative activities of two samples with different site distributions should also change dramatically in this temperature range. At higher temperatures, however, all sites might exist in more positive-order regimes and no apparent structure sensitivity may be observed.

The differences in the CO desorption rate constants between the two types of sites in a sample represent differences in desorption activation energies of 4 kcal/mol for the nitrate simulation and 5.5 kcal/mol for the chloride simulation, assuming equal pre-exponential factors. McCabe and Schmidt (*67*) have shown different crystal planes of Pt to span this difference in activation energies for desorption. What may appear to be a large difference in desorption rate constants between the two types of sites in a sample is actually consistent with the range of activation energies reported for CO desorption from Pt.

Effects of Diffusion on Dynamic Response

Figure 10 shows the evolution of the gas phase CO profiles inside the pellet for the dynamic simulation of the chloride sample shown in Fig. 8. Figures 11 and 12 show surface coverage profiles for both type-1 and type-2 sites at various times during the CO-

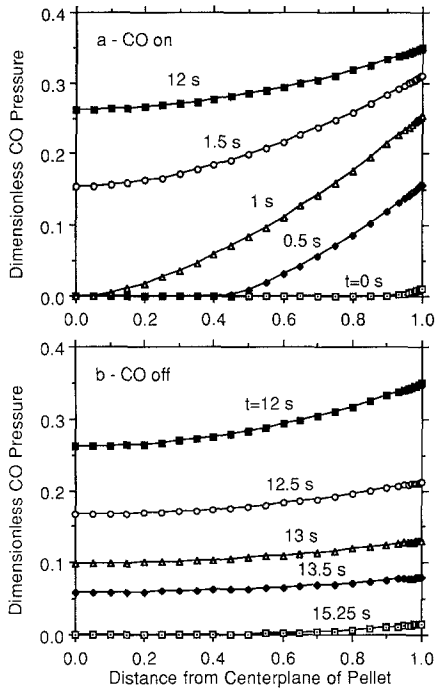

FIG. 10. Evolution of gas-phase CO profiles for the dynamic simulation of the chloride sample behavior shown in Fig. 8. The horizontal scale corresponds to the 0.19-mm half-thickness of the pellet.

on and CO-off half-periods, respectively. The horizontal span of the plots in Figs. 10–12 corresponds to the 0.19 mm-half-thickness of the pellet. Gas phase O_2 profiles inside the pellet (not shown) are relatively flat during dynamic simulations since O_2 was in stoichiometric excess and the external O_2 pressure was held constant during CO cycling. At each time, the local curvature of the gas phase CO_2 profile inside the pellet at each position (not shown) is proportional to the local surface reaction rate ($\theta_{1CO}\theta_{1O} + \theta_{2CO}\theta_{2O}$), since the CO_2 profiles are in quasi-steady state.

The gas phase and surface concentration profiles demonstrate the effects of diffusion upon the reaction system and clarify the dynamic reaction behavior for the two catalysts. The surface coverage profiles for the nitrate sample are similar, except for faster filling by CO of type-2 sites (θ_{2CO}) during the CO-on half-period and higher CO coverages on type-2 sites at mid-cycle than those shown in Fig. 12a. These differences are attributable to stronger CO adsorption characteristics (lower CO desorption rate constant) for the type-2 sites for the nitrate simulation.

The first time frame in Fig. 11a shows surface coverages on both types of sites at the beginning (t = 0 s) and, therefore, end (t = 24 s) of each cycle. Due to strong CO adsorption on type-1 sites, steep CO surface coverage gradients exist near the external

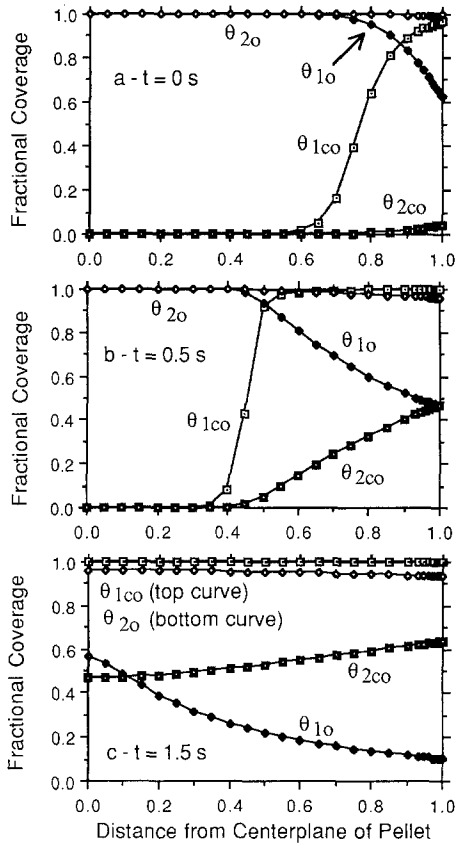

FIG. 11. Evolution of surface coverage profiles for the dynamic simulation of the chloride sample behavior during the CO-on half-period. (a) corresponds to t = 0 s, (b) to t = 0.5 s during the initial rise in CO_2 rate shown in Fig. 8, and (c) to t = 1.5 s, showing the surface profiles resulting in the first peak at t = 3.5 s in Fig. 8. The horizontal scale corresponds to the 0.19-mm half-thickness of the pellet.

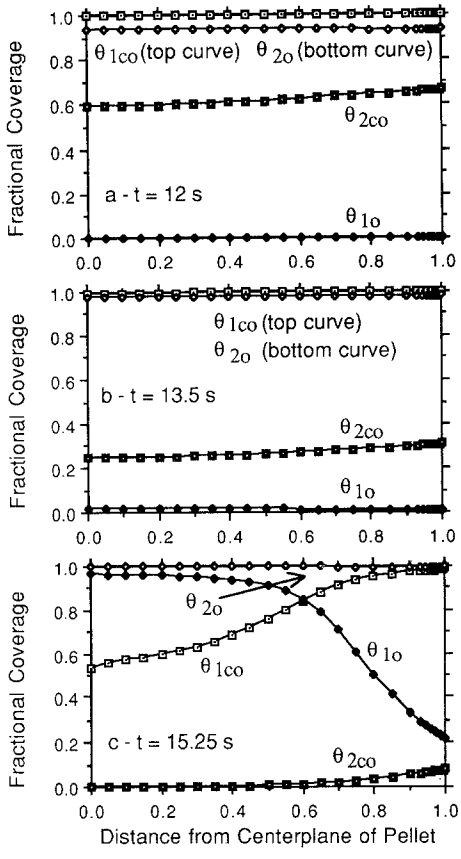

FIG. 12. Evolution of surface coverage profiles during the dynamic simulation of the chloride sample behavior during the CO-off half-period. Fig. (a) corresponds to t = 12 s, the mid-cycle rate, (b) to t = 13.5 s during the decline in CO_2 rate, and (c) to t = 15.25 s, showing the surface behavior resulting in the second peak at t = 16 s in Fig. 8. The horizontal scale corresponds to the 0.19-mm half-thickness of the pellet.

surface on type-1 sites (θ_{1CO}). Type-1 sites adsorb most of the small amount of available gas-phase CO, so type-2 sites show only a small CO surface coverage (θ_{2CO}) near the external surface. Oxygen coverages are near saturation for both types of surface sites throughout the pellet except on type-1 sites (θ_{1O}) near the external surface, where oxygen coverages are reduced due to reaction with adsorbed CO.

As gas-phase CO increases at the external surface after CO is switched on, gaseous CO begins to diffuse and adsorb at greater distances inside the pellet. Figure 11b shows the surface coverages for t = 0.5 s during the dynamic simulation shown in Fig. 8. The steep gradient in CO coverage on type-1 sites (θ_{1CO}) halfway through the pellet results from strong adsorption of CO on type-1 sites, with saturation occurring as rapidly as CO gas diffuses inside the pellet. CO coverages are near saturation where CO gas has diffused inside the pellet and near zero elsewhere. For type-1 sites, oxygen coverage (θ_{1O}) decreases almost linearly from the distance which CO gas has diffused inside the pellet to the outer surface. For type-2 sites, CO adsorption is weaker, resulting in an almost linear gradient in CO coverage (θ_{2CO}) from the external surface of the pellet to the distance inside the pellet where CO gas has diffused. Little change in oxygen coverage on type-2 sites (θ_{2O}) is predicted at t = 0.5 s.

Diffusion suppresses the rate of CO_2 production during the CO-on half-period, especially for cases of strong CO adsorption. In the absence of diffusional limitations, rapid reaction of the adsorbed oxygen layer at the beginning of each cycle would result due to rapid saturation of the entire internal surface by CO. In Fig. 11b, since the internal region of the surface is excluded from CO adsorption due to diffusional limitations, this region does not participate in the reaction at early times.

The parameter β in Eqs. (1)–(3) can be considered a dimensionless dynamic diffusivity and provides an estimate of the time frame during which diffusion suppresses the rate of CO_2 production at the start of the cycles. Assuming an infinite local rate of CO adsorption until saturation and no CO desorption, the diffusion-limited time for filling the active surface of the catalyst with adsorbed CO in the absence of reaction can be calculated (*75*). The dimensionless dynamic diffusivity β is related to the diffusion-limited surface-filling time for CO, t_{CO}, by the expression

$$t_{CO} = \frac{1}{2\beta}\left[\frac{k_{sr}Nc'^{O}_{O_2}}{c'^{O}_{CO}}\right]. \qquad (23)$$

For the simulations presented here, the diffusion-limited surface-filling time for CO is on the order of 3–5 s. Since the dimensionless dynamic diffusivity β contains the gas-to-surface capacity ratio α, the diffusion-limited surface-filling time for an adsorbing species is longer than the characteristic diffusion time of a nonadsorbing species.

Intrapellet diffusion must be considered when modeling dynamic responses during transient periods of the same order of magnitude as the diffusion-limited surface-filling times. This can be true even when diffusion resistance is negligible under steady-state conditions, since transient filling of the surface can be faster, with respect to diffusion, than steady-state reaction rates.

Between $t = 0.5$ s and $t = 1.5$ s, rapid changes occur on the surface of the catalyst. Throughout the pellet, type 1 sites become saturated with CO (θ_{1CO}) and oxygen coverages (θ_{1O}) decline, as seen in Fig. 11c. Type-1 sites reach a maximum in rate between $t = 0.5$ s and $t = 1.5$ s. However, the overall surface rate maximum does not occur until $t = 1.5$ s, since type-2 sites also contribute. At $t = 1.5$ s, the reaction rate over type-2 sites is increasing as sites continue to fill with CO (θ_{2CO}). The sum of the two surface reaction rates is a maximum at this point, since the reaction rate from type-1 sites is still large, though decreasing, at $t = 1.5$ s. At later times, rate increases are minimal on type-2 sites, since type-2 sites have almost reached steady-state coverages at $t = 1.5$ s. The reaction rate on type-1 sites decreases until type-1 sites are devoid of oxygen (θ_{1O}). This large decrease in reaction rate on type-1 sites more than offsets a small increase in rate over the type-2 sites between $t = 1.5$ s and $t = 12$ s. The virtual absence of surface gradients at 12 s (Fig. 12a) is in stark contrast to the steep gradients in CO coverage at $t = 0.5$ s. The virtual absence of surface coverage gradients at $t = 12$ s indicates that diffusional limitations are not significant under steady-state conditions at relatively high CO pressures.

Diffusion resistance does not significantly affect the rate of CO_2 production during the CO-off half-period since both reactants, adsorbed CO and O, are already present inside the pellet when CO is shut off. When CO gas is removed from the external surface, the CO_2 production rate decreases. Any remaining CO in the gas phase is adsorbed on type-1 sites, maintaining near saturation coverage of CO (θ_{1CO}) and near zero coverage of O (θ_{1O}). The CO coverage remains high and the rate stays low on type-1 sites until the CO pressure drops to a relatively low value. Since little gas-phase CO is left to adsorb on type-2 sites, the CO coverage on these sites decreases (θ_{2CO} in Fig. 12b). The overall rate decreases in conjunction with the decrease in CO surface coverage on the type-2 sites. Once CO reacts away from the type-2 sites, CO occupying type-1 sites begins to react (Fig. 12c), resulting in the second CO_2 peak at 16 s. Type-2 sites contribute little to the overall rate at this time. The maximum in overall reaction rate in the second CO_2 peak occurs as oxygen coverage increases and CO coverage decreases on type-1 sites (Fig. 12c). As time progresses, the CO coverage on type-1 sites continues to decrease. The decrease is more rapid near the center of the pellet because of reaction, resulting in the profiles shown in Fig. 11a ($t = 0$ and 24 s).

For the two-site model, uniform distribution of both types of sites is assumed throughout the pellet. Since the effect of diffusion on dynamic response was not extremely large in the simulations, similar results might be obtained if the two sites were spatially segregated from each other. However, since the differences between the sites are predicted to result from small differences in the strength of CO adsorption, which are expected to be present even over single Pt crystallites, we expect that the two sites are present together and are distributed fairly uniformly throughout the catalyst. Future experiments should be designed to differentiate between these two alterna-

tives since, as we discussed previously (*31*), spatial nonuniformities in catalyst pellets may be a common problem in kinetic studies.

The surface coverages for the two-site model shown in Figs. 11 and 12 exhibit hysteresis in the distribution of CO between the two sites. At similar total coverages, the distribution of CO is skewed toward one type of site or the other, depending on previous cycling history. This hysteresis in surface coverage demonstrates that the two-site model is not equivalent to a single-site model with coverage-dependent parameters.

The two-site model also predicts "segregation" of CO preferentially on type-1 sites at high CO pressures during dynamic operation (Fig. 12b and 12c). Segregation of CO into patches or islands was previously proposed to explain the results of steady-state and dynamic behavior for CO oxidation (*38*). Evidence to support the existence of CO islands on supported noble metals during reaction is primarily limited to FTIR measurements of CO frequency invariances with changing total CO surface coverage. In a previous work (*31*), we proposed that segregation of CO into patches or islands could potentially explain the appearance of the CO_2 peaks during dynamic cycling. However, we found that models incorporating CO islands with very complex perimeter specifications could only approximate the features of the experimental dynamic responses (*76, 77*).

Previously proposed mechanisms of Pt oxidation and reduction are applicable to long transients and oscillatory behavior (*5, 75*). Previously proposed surface reconstruction models (*23, 51*) cannot qualitatively explain the dynamic behavior we have observed (*31*). The two-site model requires additional specification of only three parameters to a traditional L–H model in order to predict the steady-state and dynamic behavior observed over the two Pt/Al_2O_3 catalysts. In addition, segregation of CO on strong CO adsorption sites with limited reaction, in conjunction with reaction of co-adsorbed CO and oxygen on weaker CO binding sites, might account for the observed invariance of CO frequency with changing surface coverage previously attributed to the formation of CO islands.

CONCLUSIONS

In this work, we have demonstrated that traditional Langmuir–Hinshelwood models of CO oxidation cannot predict the steady-state and dynamic behavior observed over our Pt/Al_2O_3 catalysts. A kinetic model that specifies a bimodal distribution of active sites with different activities and adsorption characteristics was able to explain most of the experimental results with specification of only three additional parameters. This work demonstrates that site heterogeneity should be considered along with segregation of adsorbates and surface phase transformations as possible explanations of steady-state and dynamic CO oxidation kinetics.

Intrapellet diffusion will affect the dynamic response of a catalyst when cycling periods are the same order of magnitude as diffusion-limited surface-filling times. Significant internal concentration gradients were present in our experiments under steady-state conditions of low CO/O_2 ratio and during transient filling of the surface by CO. Diffusion resistance modified the shape and size of the initial CO_2 peaks formed during dynamic cycling of CO, but did not cause the appearance of any of the CO_2 peaks observed.

APPENDIX: NOTATION

Subscripts

i	Index for product and reactant species (CO, O_2, O, CO_2)
j	Index for type of site (1, 2)

Variables, Parameters, and Parameter Values

c_i'	Concentration of species i in gas phase within the pellet (mol/cm^3)
$c_{CO}'^{O}$	Concentration of CO in gas phase external to the pellet = 4.795×10^{-9} mol/cm^3
$c_{O_2}'^{O}$	Concentration of O_2 in gas phase external to the pellet = 1.266×10^{-8} mol/cm^3
$c_{CO_2}'^{O}$	Concentration of CO_2 in gas phase external to the pellet = 0.0 mol/cm^3
D_e	Effective diffusivity = 2.25 cm^2/s
ε_p	Void fraction of porous catalyst pellet = 0.3
k_{aCO}	Adsorption rate constant for CO (cm^3/mol · s)
k_{aO_2}	Adsorption rate constant for O_2 (cm^5/mol^2 · s)
k_{dCO}	Desorption rate constant for CO (s^{-1})
k_{sr}	Surface reaction rate constant (cm^2/mol · s)
k_{ajCO}	Adsorption rate constant on site j for CO (cm^3/mol · s)
k_{ajO_2}	Adsorption rate constant on site j for O_2 (cm^5/mol^2 · s)
k_{djCO}	Desorption rate constant on site j for CO (s^{-1})
k_{srj}	Surface reaction rate constant on site j (cm^2/mol · s)
L	Half-thickness of slab-geometry catalyst pellet = 0.019 cm
n_i	Surface concentration of species i on active area (mol/cm^2)
n_{ji}	Surface concentration on site j of species i (mol/cm^2)
n_j	Concentration of site j in active area (mol/cm^2)
N	Total concentration of active sites in active area = 2.0×10^{-9} mol/cm^2
S_p	Active area to pellet volume ratio = 1.58×10^4 cm^2/cm^3
t	Time (s)
x'	Distance from the centerplane of the slab-geometry catalyst pellet (cm)

Dimensionless Rates of Elementary Steps

r_{aCO}	Adsorption rate of CO
r_{aO_2}	Adsorption rate of O_2
r_{dCO}	Desorption rate of CO
r_{sr}	Surface reaction rate between adsorbed O and CO
r_{ajCO}	Adsorption rate on site j of CO
r_{ajO_2}	Adsorption rate on site j of O_2
r_{djCO}	Desorption rate on site j of CO
r_{srj}	Surface reaction rate on site j between adsorbed O and CO

Dimensionless Variables, Parameters, and Parameter Values

c_i	$= c_i'/c_{O_2}'^{O}$	Dimensionless gas concentration in pores of species i
c_i^O	$= c_i'^{O}/c_{O_2}'^{O}$	Dimensionless gas concentration in pores of species i at the external face of the pellet
f_j	$= n_j/N$	Fraction of total sites which are type-j sites
r_{CO_2}	$= -\beta[\partial c_{CO_2}/\partial x]_{x=1}$	Dimensionless instantaneous rate of diffusion of CO_2 out of the pellet
x	$= x'/L$	Dimensionless distance from centerplane of pellet

α	$= \varepsilon_p c'^{O}_{O_2}/(S_p N)$	Pore gas concentration to surface concentration ratio, "gas-to-surface capacity ratio" $= 1.2 \times 10^{-4}$
β	$= \alpha D_e/(k_{sr} N L^2)$	Dimensionless dynamic diffusivity
γ_{aCO}	$= k_{aCO} c'^{O}_{O_2}/(k_{sr} N)$	Dimensionless adsorption rate constant for CO
γ_{aO_2}	$= k_{aO_2} c'^{O}_{O_2}/k_{sr}$	Dimensionless adsorption rate constant for O_2
γ_{dCO}	$= k_{dCO}/(k_{sr} N)$	Dimensionless desorption rate constant for CO
γ_{ajCO}	$= k_{ajCO} c'^{O}_{O_2}/(k_{sr1} N)$	Dimensionless adsorption rate constant on site j for CO
γ_{ajO_2}	$= k_{ajO_2} c'^{O}_{O_2}/k_{sr1}$	Dimensionless adsorption rate constant on site j for O_2
γ_{djCO}	$= k_{djCO}/(k_{sr1} N)$	Dimensionless desorption rate constant on site j for CO
γ_{srj}	$= k_{srj}/k_{sr1}$	Dimensionless reaction rate constant on site j
θ_i	$= n_i/N$	Fractional surface coverage of species i
θ_{ji}	$= n_{ji}/n_j$	Fractional surface coverage on site j of species i
τ	$= t k_{sr} N$	Dimensionless time ($= t k_{sr1} N$ for two-site model)

ACKNOWLEDGMENTS

Andrew F. Cannestra performed the CO_2/Ar experiments demonstrating the negligible adsorption of CO_2 on the catalysts. The National Science Foundation supported this work through Grant CBT-87-15427.

REFERENCES

1. Wei, J., *Adv. Chem. Ser.* **148,** 1 (1975).
2. Hegedus, L. L., Oh, S. E., and Baron, K., *AIChE J.* **23,** 632 (1977).
3. Golchet, A., and White, J. M., *J. Catal.* **53,** 266 (1978).
4. Haaland, D. M., and Williams, F. L., *J. Catal.* **76,** 450 (1982).
5. Sales, B. C., Turner, J. E., and Maple, M. B., *Surf. Sci.* **103,** 54 (1981).
6. Rathousky, J., and Hlavacek, V., *J. Catal.* **75,** 122 (1982).
7. Böcker, D., and Wicke, E., *in* "Temporal Order" (L. Rensing and N. I. Jaeger, Eds.), p. 75. Springer-Verlag, Berlin, 1984.
8. Lynch, D. T., and Wanke, S. E., *J. Catal.* **88,** 333 (1984).
9. Razon, L. F., Chang, S.-M., and Schmitz, R. A., *Chem. Eng. Sci.* **41,** 1561 (1986).
10. Sant, R., and Wolfe, E. E., *J. Catal.* **110,** 249 (1988).
11. Ertl, G., Norton, P. R., and Rusting, J., *Phys. Rev. Lett.* **49,** 177 (1982).
12. Cox, M. P., Ertl, G., and Imbihl, R., *Phys. Rev. Lett.* **54,** 1725 (1985).
13. Cutlip, M. B., *AIChE J.* **25,** 502 (1979).
14. Barshad, Y., and Gulari, E., *AIChE J.* **31,** 649 (1985).
15. Barshad, Y., Zhou, X., and Gulari, E., *J. Catal.* **94,** 128 (1985).
16. Zhou, X., Barshad, Y., and Gulari, E., *Chem. Eng. Sci.* **41,** 1277 (1986).
17. Zhou, X., and Gulari, E., *Langmuir* **2,** 715 (1986).
18. Engel, T., and Ertl, G., *Adv. Catal.* **28,** 1 (1979).
19. Kaul, D. J., and Wolf, E. E., *J. Catal.* **89,** 348 (1984).
20. Harold, M. P., and Luss, D., *Chem. Eng. Sci.* **40,** 39 (1985).
21. Harold, M. P., and Luss, D., *Ind. Eng. Chem. Res.* **26,** 2099 (1987).
22. Graham, W. R. C., and Lynch, D. T., *in* "Studies in Surface Science and Catalysis" (J. W. Ward, Ed.), Vol. 38, p. 693. Elsevier, Amsterdam, 1988.
23. Graham, W. R. C., and Lynch, D. T., *AIChE J.* **36,** 1796 (1990).
24. Lindstrom, T. H., and Tsotsis, T. T., *Surf. Sci.* **171,** 349 (1986).
25. Cant, N. W., Hicks, P. C., and Lennon, B. S., *J. Catal.* **54,** 372 (1978).
26. Oh, S. H., Fisher, G. B., Carpenter, J. E., and Goodman, D. W., *J. Catal.* **100,** 360 (1986).
27. Sarkany, J., and Gonzalez, R. D., *Appl. Catal.* **5,** 85 (1983).
28. Akubuiro, E. C., Verykios, X. E., and Lesnick, L., *Appl. Catal.* **14,** 215 (1985).
29. Bennett, C. O., *Catal. Rev.-Sci. Eng.* **13,** 121 (1976).
30. Kobayashi, M., and Kobayashi, H., *Catal. Rev.-Sci. Eng.* **10,** 139 (1974).
31. Racine, B. N., Sally, M. J., Wade B., and Herz, R. K., *J. Catal.* **127,** 307 (1991).
32. Goodman, M. G., Cutlip, M. B., Kenney, C. N., Morton, W., and Mukesh, D., *Surf. Sci.* **120,** L453 (1982).
33. Kaul, D. J., Sant, R., and Wolf, E. E., *Chem. Eng. Sci.* **42,** 1399 (1987).
34. Lynch, D. T., *Chem. Eng. Sci.* **39,** 1325 (1984).
35. Cant, N. W., and Donaldson, R. A., *J. Catal.* **71,** 320 (1981).
36. Shigeishi, R. A., and King, D. A., *Surf. Sci.* **75,** L397 (1978).
37. Li, Y.-E., Böcker, D., and Gonzalez, R. D., *J. Catal.* **110,** 319 (1988).
38. Mukesh, D., Morton, W., Kenney, C. N., and Cutlip, M. B., *Surf. Sci.* **138,** 237 (1984).

39. Graham, W. R. C., and Lynch, D. T., *Surf. Sci.* **187,** L633 (1987).
40. Dumont, M., Poraiux, M., and Dagonnier, R., *Surf. Sci.* **169,** L307 (1986).
41. Ziff, R. M., Gulari, E., and Barshad, Y., *Phys. Rev. Lett.* **56,** 2553 (1986).
42. Araya, P., Porod, W., and Wolf, E. E., *Surf. Sci.* **230,** 245 (1990).
43. Silverberg, M., Ben-Shaul, A., and Rebentrost, F., *J. Chem. Phys.* **83,** 6501 (1985).
44. Silverberg, M., and Ben-Shaul, A., *J. Chem. Phys.* **87,** 3178 (1987).
45. Fichthorn, K. A., Ziff, R. A., and Gulari, E., *in* "Studies in Surface Science and Catalysis" (J. W. Ward, Ed.) Vol. 38, p. 883. Elsevier, Amsterdam, 1988.
46. Schwartz, S. B., and Schmidt, L. D., *Surf. Sci.* **183,** L269 (1987).
47. Ladas, S., Imbihl, R., and Ertl, G., *Surf. Sci.* **198,** 42 (1988).
48. Thiel, P. A., Behm, R. J., Norton, P. R., and Ertl, G., *Surf. Sci.* **121,** L553 (1982).
49. Behm, R. J., Theil, P. A., Norton, P. R., and Ertl, G., *J. Chem. Phys.* **78,** 7437 (1983).
50. Schüth, F., and Wicke, E., *Ber. Bunsenges Phys. Chem.* **93,** 191 (1989).
51. Lynch, D. T., Emig, G., and Wanke, S. E., *J. Catal.* **97,** 456 (1986).
52. Oh, S. E., and Hegedus, L. L., *in* "Catalysis under Transient Conditions," (A. T. Bell and L. L. Hegedus, Eds.), ACS Symposium Series, Vol. 178. American Chemical Society, Washington, DC, 1982.
53. Oh, S. E., Baron, K. B., Cavendish, J. C., and Hegedus, L. L., *ACS Symp. Ser.* **65,** 461 (1978).
54. Cho, B. K., *Ind. Eng. Chem. Fundam.* **22,** 410 (1983).
55. Sant, R., and Wolf, E. E., *Surf. Sci.* **187,** 511 (1987).
56. Kaul, D. J., and Wolf, E. E., *J. Catal.* **93,** 321 (1985).
57. Gland, J. L., and Korchak, V. N., *Surf. Sci.* **75,** 733 (1978).
58. Herz, R. K., and Marin, S. P., *J. Catal.* **65,** 281 (1980).
59. Bennett, C. O., Laporta, L. M., and Cutlip, M. B., *in* "Studies in Surface Science and Catalysis" (A. Crucq and A. Frennet, Eds.), Vol. 30, p. 143. Elsevier, Amsterdam, 1987.
60. Dwyer, S. M., and Bennett, C. O., *J. Catal.* **75,** 275 (1982).
61. Harold, M. P., and Garske, M. E., *J. Catal.* **127,** 524 (1991).
62. Tsai, P. K., Wu, M. G., and Maple, M. B., *J. Catal.* **127,** 512 (1991).
63. Conrad, H., Ertl, G., and Küppers, J., *Surf. Sci.* **76,** 323 (1978).
64. Ramachandran, A. S., Anderson, S. L., and Datye, A. K., in preparation.
65. Datye, A. K., Logan, A. D., and Long, N. J., *J. Catal.* **109,** 76 (1988).
66. Altman, E. I., and Gorte, R. J., *Surf. Sci.* **172,** 71 (1986).
67. McCabe, R. W., and Schmidt, L. D., *Surf. Sci.* **66,** 101 (1977).
68. Norton, P. R., Goodale, J. W., and Selkirk, E. B., *Surf. Sci.* **83,** 189 (1979).
69. Matolin, V., Gillet, E., and Channakhone, S., *J. Catal.* **97,** 448 (1986).
70. Yao, H. C., Sieg, M., and Plummer, Jr., H. K., *J. Catal.* **59,** 365 (1979).
71. Oukaci, R., Gallaher, G., Goodwin, J. G., and Blackmond, D. G., presented at Fourth Chem. Cong. of N. Amer., New York, NY, Aug. 25–30, 1991.
72. McCarthy, E., Zahradnik, J., Kuczynski, G. C., and Carberry, J. J., *J. Catal.* **39,** 29 (1975).
73. Herskowitz, M., Holliday, R., Cutlip, M. B., and Kenney, C. N., *J. Catal.* **74,** 408 (1982).
74. Cant, N. W., *J. Catal.* **62,** 173 (1982).
75. Herz, R. K., and Shinouskis, E. J., *Appl. Surf. Sci.* **19,** 373 (1984).
76. Racine, B. N., Ph.D. Dissertation, University of California, San Diego, 1991.
77. Racine, B. N., and Herz, R. K., Paper No. 48a, presented to Am. Inst. Chem. Eng., San Francisco, Nov. 1989.